Faculty Publications from the Department of Electrical and Computer Engineering

Electrical & Computer Engineering, Department of

2015

An Isolated Three-Port Bidirectional DC-DC Converter for Photovoltaic Systems with Energy Storage

Jianwu Zeng
University of Nebraska-Lincoln, jzeng@huskers.unl.edu

Wei Qiao
University of Nebraska-Lincoln, wqiao@engr.unl.edu

Liyan Qu
University of Nebraska-Lincoln, lqu2@unl.edu

An Isolated Three-Port Bidirectional DC-DC Converter for Photovoltaic Systems with Energy Storage

Jianwu Zeng, *Student Member, IEEE*, Wei Qiao, *Senior Member, IEEE*, and Liyan Qu, Member, *IEEE*

Abstract—**This paper proposes a new isolated, three-port, bidirectional, DC-DC converter for simultaneous power management of multiple energy sources. The proposed converter has the advantage of using the least number of switches and soft switching for the main switch, which is realized by using a LCL-resonant circuit. The converter is capable of interfacing sources of different voltage-current characteristics with a load and/or a DC microgrid. The proposed converter is constructed for simultaneous power management of a photovoltaic (PV) panel, a rechargeable battery, and a load. Simulation and experimental results show that the proposed converter is capable of maximum power point tracking control for the PV panel when there is solar radiation and controlling the charge and discharge of the battery when there is surplus energy and power deficiency with respect to the load, respectively.**

Index Terms—**Battery, bidirectional DC-DC converter, isolated converter, multiport converter, photovoltaic (PV), soft switching, zero-current switching (ZCS).**

I. INTRODUCTION

To integrate multiple DC energy sources of different types to a power grid, multiple independent DC-DC converters are commonly used to step up the time-variant, low-level source voltages to a constant high-level voltage that is required by a grid-tie inverter. Comparing to that solution, a multiport DC-DC converter is preferable owing to the advantages of using fewer components, lower cost, higher power density, and higher efficiency [1], [2].

The multiport converter topologies can be classified into two categories: nonisolated and isolated topologies [3]. Nonisolated multiport converters are usually used in the applications where a low voltage regulation ratio is required [4], [5]. In contrast, in the applications requiring a high voltage regulation ratio, isolated converters which contains a transformer is preferred [6]-[8].

The authors are with the Power and Energy Systems Laboratory, Department of Electrical and Computer Engineering, University of Nebraska-Lincoln, Lincoln, NE 68588-0511 USA (e-mail: jzeng@huskers.unl.edu; wqiao@engr.unl.edu; lqu2@unl.edu)

The currently used isolated multiport topologies include the isolated full-bridge converter [6], which uses four controllable power switches for each source, the isolated half-bridge converter [9], which uses two switches for each source, and the isolated single-switch converter [10], which only uses one switch for each source. In some practical applications, energy storage, such as batteries, is commonly used to handle the intermittence of solar and wind energy sources. This requires that at least one port of the multiport converter is bidirectional. The aforementioned topologies are all unidirectional and cannot satisfy such applications [11].

Several bidirectional topologies, such as full-bridge [12], [13] and half-bridge [14], [15] topologies, have been proposed. These two topologies utilize many switches with complicated drive and control circuits. Recently, a three-port topology was proposed by adding one middle branch to the traditional half-bridge converter [16], [17]. It uses less controllable power switches than the half-bridge topology and can achieve zero-voltage switching (ZVS) for all main switches. However, the voltage of the primary source should be maintained at a high value to charge the battery and the battery is both charged and discharged within a switching period. Such a high-frequency charge/discharge has a negative effect on the battery lifetime.

This paper proposes a new isolated, three-port, bidirectional, DC-DC converter. It contains an inductor-capacitor-inductor (LCL)-resonant circuit to achieve zero-current switching (ZCS) for the main switch. Compared with the converter in [17] using five controllable switches, the proposed converter only use three switches; moreover, when using the same renewable energy source to charge a battery, the nominal voltage of the battery connected to the proposed converter can be higher than that connected to the converter in [17]. The proposed converter is applied for simultaneous power management of a photovoltaic (PV) system with a battery in this paper. The PV system and the battery are connected to the unidirectional port and the bidirectional port of the converter, respectively. A maximum power point tracking (MPPT) algorithm is designed for the PV panel to generate the maximum power when solar radiation is available. A charge and discharge controller is designed to control the battery to either absorb the surplus power generated by the PV panel or supply the deficient power required by the load. Simulation and experimental results are provided to validate the proposed converter.
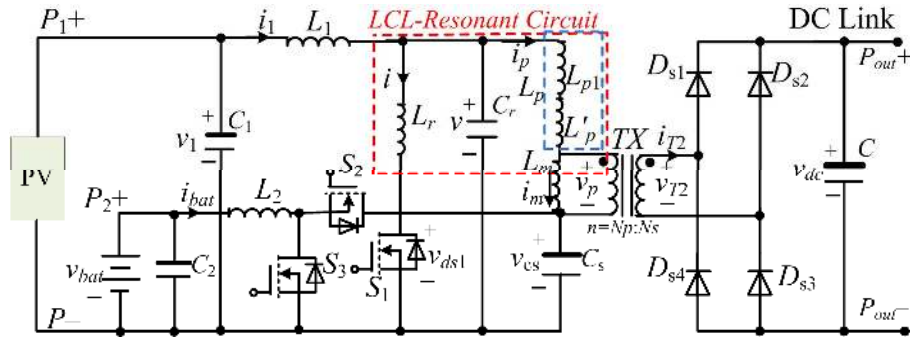
Fig. 1. Proposed isolated, three-port, bidirectional, DC-DC converter for a PV and battery system.

II. TOPOLOGY AND OPERATING PRINCIPLE OF THE PROPOSED CONVERTER

A. Topology of the Proposed Converter

The circuit diagram of the proposed converter is shown in Fig. 1, which consists of a low-voltage-side (LVS) circuit and a high-voltage-side (HVS) circuit connected by a high-frequency transformer. The LVS consists of two ports, an energy storage capacitor C_s, the primary winding of the transformer, and a LCL-resonant circuit consisting of two inductors L_r and L_p and a capacitor C_r, where L_p includes the added inductance L_{p1} and the leakage inductance of the transformer L'_p. The HVS consists of the secondary winding of the transformer and a full-bridge rectifier implemented with the diodes $D_{s1} \sim D_{s4}$. The transformer's turn ratio is defined as: $n = N_p / N_s$, where N_p and N_s represent the numbers of turns of the primary and secondary windings, respectively. Among the switches, S_1 is called the main switch because it not only controls the power generated by the source connected to Port 1 (P_1), but also changes the direction of the current flowing through the transformer.

In this paper, the two ports on the LVS are connected to a PV panel and a battery. To simplify the analysis, the proposed converter is analyzed by two separate converters: one is a single-switch LCL-resonant converter [18], and the other is the battery-related buck and boost converter consisting of L_2, S_2, and S_3.

B. Single-Switch LCL-Resonant Converter for PV Panel

In a switching period, the voltages across C_1 and C_s can be taken as constant values. Particularly, in the steady state, $V_{Cs} = V_1$, where V_1 is the output voltage of the PV panel. The converter has seven operating modes depending on the states of the switch S_1 and the resonant circuit. Fig. 2 shows the equivalent resonant circuit in different modes. The differential equations of the resonant circuit in Mode k ($k = 1, \cdots, 7$) are

$$\begin{cases} v = L_r^{(k)} \cdot \dfrac{di_r^{(k)}}{dt} \\ i_1 = C_r \cdot \dfrac{dv}{dt} + i_r^{(k)} \end{cases} \quad (1)$$

where v represents the voltage of the capacitor C_r; $L_r^{(k)}$ and $i_r^{(k)}$ represents the equivalent resonant inductance and the current through the equivalent resonant inductor in the kth ($k = 1, \cdots, 7$)

operating mode, respectively. Then v can be solved from (1) and has the following form.

$$v(t) = A^{(k)} \cos\left[\omega^{(k)}(t - t_k)\right] + B^{(k)} \sin\left[\omega^{(k)}(t - t_k)\right] + V^{(k)} \quad (2)$$

where

$$\omega^{(k)} = 1 / \sqrt{L_r^{(k)} \cdot C_r} \quad (3)$$

is the resonant frequency in Mode k; $V^{(k)}$ is the particular solution of equation (1) in Mode k, and $A^{(k)}$ and $B^{(k)}$ are coefficients, which can be expressed as:

$$A^{(k)} = v(t_k) - V^{(k)} \quad (4)$$

$$B^{(k)} = \frac{I_1 - i_p(t_k) - i(t_k)}{\omega^{(k)} \cdot C_r} \quad (5)$$

where $v(t_k)$, I_1, $i_p(t_k)$, and $i(t_k)$ represent the voltage across C_r and the currents of L_1 (i_1 can be viewed as a constant value I_1 because of a large L_1), L_p, and L_r at time t_k, respectively. Equations (4) and (5) indicate that only $\omega^{(k)}$ and $V^{(k)}$ are required to determine the parameters of (2).

The steady-state waveforms and equivalent circuits of the seven operating modes of the converter are shown in Figs. 3 and 4, respectively. To facilitate the explanation of the converter operation, define $V_T = n \cdot V_{dc}$ the equivalent output voltage of the converter referred to the primary side of the transformer.

Mode 1: $t \in [t_1, t_2]$ (see Fig. 3). Prior to Mode 1, S_1 is off; the currents through L_r and L_p are zero and a positive value of I_1, respectively, i.e., $i(t_1) = 0$, $i_p(t_1) = I_1$. When S_1 is on, as shown in Fig. 4(a), L_r and L_p resonate with C_r, the current of the inductor L_r increases and the voltage of the capacitor C_r decreases. Due to the existence of L_r, the current through the switch S_1 increases slowly so that the switch is turned on under a low di/dt condition. The resonant frequency and the particular solution in this mode can be expressed as:

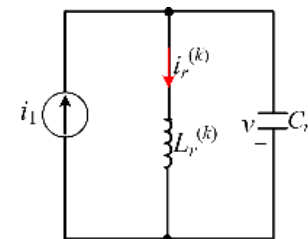$$\omega^{(1)} = 1 / \sqrt{(L_r // L_p) \cdot C_r} \quad (6)$$

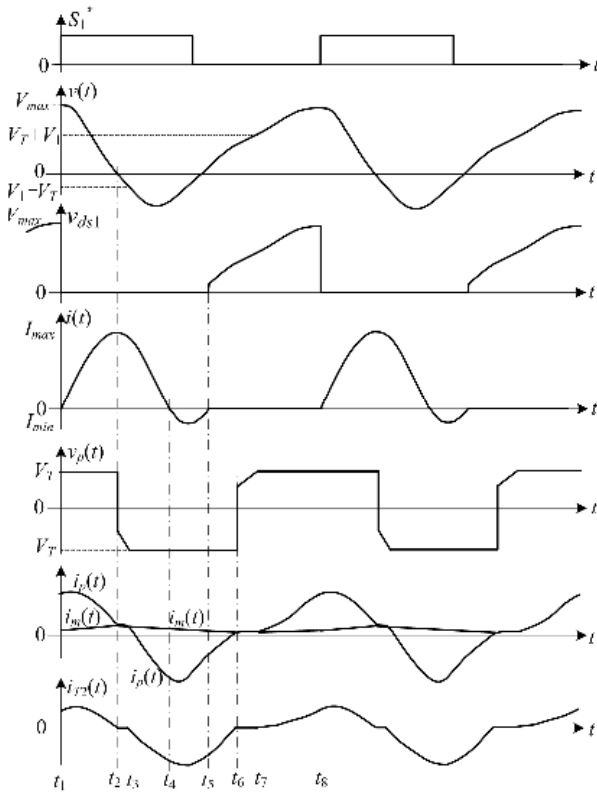
Fig. 2. Equivalent resonant circuit.

Fig. 3. Steady-state waveforms of the proposed converter.

$$V^{(1)} = \frac{L_r}{L_r + L_p} \cdot (V_1 + V_T) \tag{7}$$

where // represents that L_r and L_p are connected in parallel. In this mode, the current i_m through the primary magnetizing inductance L_m increases, the current i_{T2} through the secondary

side of the transformer is positive, which indicates the conduction of the D_{s1} and D_{s3}. At the end of Mode 1, $i_p(t_2) = i_m(t_2)$, i achieves its maximum value I_{max}, $i_{T2}(t_2) = 0$, $v(t_2) = 0$, and v_p changes its polarity from positive to negative.

Mode 2: $t \in [t_2, t_3]$, during which S_1 is on, $i(t) > 0$, and $i_p(t) = i_m(t)$, $D_{s1}-D_{s4}$ are reverse biased such that $i_{T2} = 0$. As shown in Fig. 4(b), L_m, L_p, and L_r resonate with C_r.

Since $L_m \gg L_p$, $L_m \gg L_r$, then

$$\omega^{(2)} = 1/\sqrt{[(L_p + L_m)//L_r] \cdot C_r} \approx 1/\sqrt{L_r \cdot C_r} \tag{8}$$

$$V^{(2)} = \frac{L_r}{L_r + L_p + L_m} \cdot V \approx \frac{L_r}{L_m} \cdot V_1 \tag{9}$$

At the end of Mode 2, $v_p(t_3) = -V_T$, $v(t_3) = V_1 - V_T$, the diodes D_{s2} and D_{s4} begin to conduct.

Mode 3: $t \in [t_3, t_4]$, during which S_1 is on, $i(t) > 0$, $v_p(t) = -V_T$, $i_{T2} < 0$. As shown in Fig. 4(c), L_r and L_p resonate with C_r; the energy stored in L_r is released to charge the capacitor C_r; v_p is clamped to $-V_T$; and i_{T2} is negative, which indicates the conduction of D_{s2} and D_{s4}. Compared to Mode 1, the only difference in the equivalent circuit in this mode is the sign of v_p. Thus, $\omega^{(3)} = \omega^{(1)}$, and

$$V^{(3)} = \frac{L_r}{L_r + L_p} \cdot (V_1 - V_T) \tag{10}$$

This mode terminates at time t_4 when the current of L_r decreases to zero, i.e., $i(t_4) = 0$.

Mode 4: $t \in [t_4, t_5]$, during which S_1 is on, $i(t) < 0$, $v_p(t) = -V_T$, $i_{T2} < 0$, and D_{s2} and D_{s4} conduct. As shown in Fig. 4(d), a negative current flows through the internal diode of the switch S_1; the gate signal can be removed to turn off the switch, e.g., at time t_5, under the ZCS condition. The circuit equations are the same as those in Mode 3. Thus, $\omega^{(4)} = \omega^{(1)}$, $V^{(4)} = V^{(3)}$. At the end of Mode 4, $i(t_5) = 0$ and the voltage across the switch S_1 is the
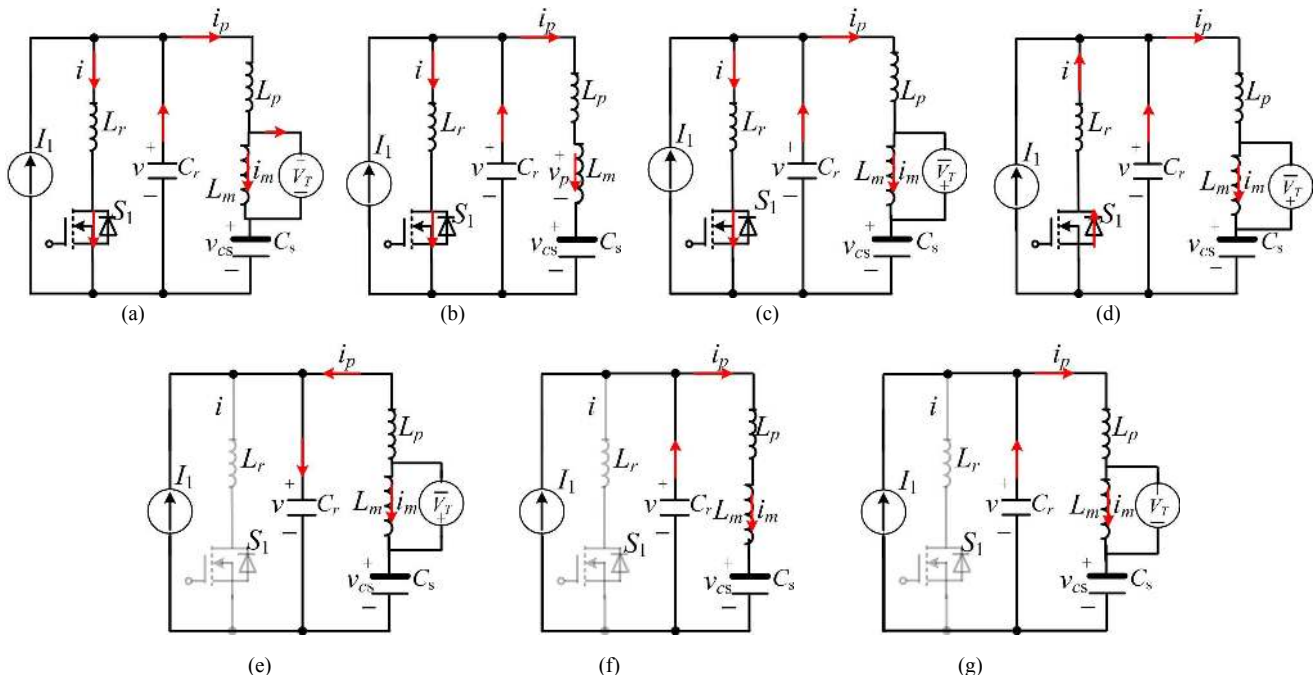

(a)   (b)   (c)   (d)

(e)   (f)   (g)

Fig. 4. Equivalent circuits for different operating modes. (a) Mode 1: S_1 is on, $i > 0$, $v_p = V_T$; (b) Mode 2: S_1 is on, $i > 0$ and $i_p = i_m$; (c) Mode 3: S_1 is on, $i > 0$, and $v_p = -V_T$; (d) Mode 4: S_1 is being turned off, $i < 0$ and $v_p = -V_T$; (e) Mode 5: S_1 is off, $i = 0$, $v_p = -V_T$; (f) Mode 6: S_1 is off, $i = 0$, $i_p = i_m$; (g) Mode 7: S_1 is off, $i = 0$, $v_p = V_T$.

same as that across the capacitor C_r, i.e., $v_{ds1}(t_5) = v$.

Mode 5: $t \in [t_5, t_6]$, during which S_1 is off, $i(t) = 0$, $v_p = -V_T$, and $i_{T2} < 0$. As shown in Fig. 4(e), L_r and the switch S_1 can be neglected in the circuit. The inductor L_p resonates with C_r, and the direction of i_p changes from negative to positive. The following can be obtained.

$$\omega^{(5)} = 1/\sqrt{L_p \cdot C_r} \tag{11}$$

$$V^{(5)} = V_1 - V_T \tag{12}$$

At the end of Mode 5, $i_p(t_6) = i_m(t_6)$, $i_{T2}(t_6) = 0$, and v_p changes its polarity from negative to positive.

Mode 6: $t \in [t_6, t_7]$, during which S_1 is off, $i(t) = 0$, $i_p(t) = i_m(t)$, $D_{s1}-D_{s4}$ are reverse biased such that $i_{T2} = 0$. As shown in Fig. 4(f), L_m and L_p resonate with C_r, and C_r is charged. The following can be obtained.

$$\omega_6 = 1/\sqrt{(L_p + L_m) \cdot C_r} \approx 1/\sqrt{L_m \cdot C_r} \tag{13}$$

$$V^{(6)} = V_1 \tag{14}$$

At time t_7, $v(t_7) = V_1 + V_T$ and $v_p(t_7) = V_T$.

Mode 7: $t \in [t_7, t_8]$, during which S_1 is off, $i(t) = 0$, $v_p(t) = V_T$, D_{s1} and D_{s3} conduct. As shown in Fig. 4(g), L_p resonates with C_r, the circuit equations are the same as those in Mode 5 except the sign of v_p, then $\omega^{(7)} = \omega^{(5)}$, and

$$V^{(7)} = V_1 + V_T \tag{15}$$

Once S_1 is turned on at time t_8, Mode 7 switches to Mode 1.

There are five inductances L_1, L_2, L_r, L_{p1}, and L_m in the proposed converter that need to be properly designed. L_m is designed based on the following critical inductance L_{mc} [18].

$$L_{mc} = \frac{V_T \cdot T}{4 \cdot I_{m,pk}} \tag{16}$$

where T is the switching period of the switch S_1; $I_{m,pk}$ is the peak current through the magnetizing inductor. In this paper, the root mean square (RMS) value of the magnetizing current is designed to be 2% of the RMS value of i_p. Then L_m is designed to be larger than L_{mc}. Once the transformer is designed, the leakage inductance L'_p of the transformer can be measured.

Given the load resistance R_L and the transformer's turn ratio n, the quality factor Q of this LCL-resonant converter can be calculated [19]:

$$Q = \frac{8 \cdot n^2 \cdot R_L}{\pi^2 \cdot Z} \tag{17}$$

where Z is the characteristic impedance of the resonant circuit defined below.

$$Z = \sqrt{\frac{L_r // (L_{p1} + L'_p)}{C_r}} \tag{18}$$

Given the desired value of Q and the value of R_L, the value of Z can be calculated from (16). In this paper, Q is selected in the optimal range of [1.5, 5]. Specifically, the value of Q is 3.7 when the nominal load is applied. Then, given the resonant frequency, C_r can be calculated from (6) and (18). Considering the necessary condition $L_p > L_r$ to achieve ZCS [20], $L_r = L_{p1}$ is selected such that the currents through the switch S_1 and the transformer are close during the resonant stage. Then L_r and L_{p1} can be calculated from (18) with the measured value of L'_p.

The values of L_1 and L_2 are designed according to their desired current ripples [10]. In this paper, it is expected that the current ripples are within 5% of their nominal currents.

C. Buck and Boost Converter for Battery

The buck and boost converter consists of the inductor L_2, switches S_2 and S_3, and capacitor C_s. When the generated solar power is larger than the power required by the load, S_3 is inactive and S_2 is switched on to form the buck converter. Then, the surplus energy generated from the PV panel is stored in the battery. In contrast, when the generated solar power is less than the power required by the load, S_2 is switched off and S_3 is switched on to form the boost converter. The battery is discharged to C_s to provide the deficient energy required by the load.

III. POWER MANAGEMENT OF THE PROPOSED CONTROLLER

Two controllers are needed to manage the power in the LVS. Their objectives are to regulate the output DC-link voltage to a constant value and manage the power for the two sources, respectively. According to the availability of the solar power, there are three working scenarios of the converter, as illustrated in Fig. 5.

A. Three Working Scenarios

Scenario 1 ($p_1 \geq p_{out}$): the available solar power is more than the load demand. As shown in Fig. 5(a), the PV converter works in the MPPT mode; the battery is charged so that the DC-link voltage is controlled at a constant value.

Scenario 2 ($0 < p_1 < p_{out}$): there is solar radiation but the solar power is not sufficient to supply the load. As shown in Fig. 5(b), the PV panel is controlled in the MPPT mode by the MPPT algorithm described later. On the other hand, the deficient power is supplied by the battery, which is discharged by the boost converter, so that the DC-link voltage can be maintained at a constant value.

Scenario 3 ($p_1 = 0$): there is no solar power available and, thus, the battery is discharged to supply the load, as shown in Fig. 5(c). The active switches are S_1 and S_3.

Proper controllers are designed to manage the power of the system in different scenarios. Fig. 6 shows the overall system with controllers, which include a MPPT controller for the PV panel and charge and discharge controllers for the battery.

B. MPPT Controller for PV Panel

The proposed converter is applied for MPPT control of a PV panel using the perturbation and observation (P&O) MPPT algorithm [21] to maximize the PV panel's output efficiency. Fig. 7 shows the flowchart of the MPPT algorithm. A ratio r_c is defined to specify the relative power change (RPC) of the PV panel between two consecutive sampling steps.

$$r_c = \frac{|P_1(k) - P_1(k-1)|}{P_1(k-1)} \tag{19}$$

where $P_1(k)$ and $P_1(k-1)$ represent the measured output power of the PV panel in the kth and $(k-1)^{th}$ steps, respectively.
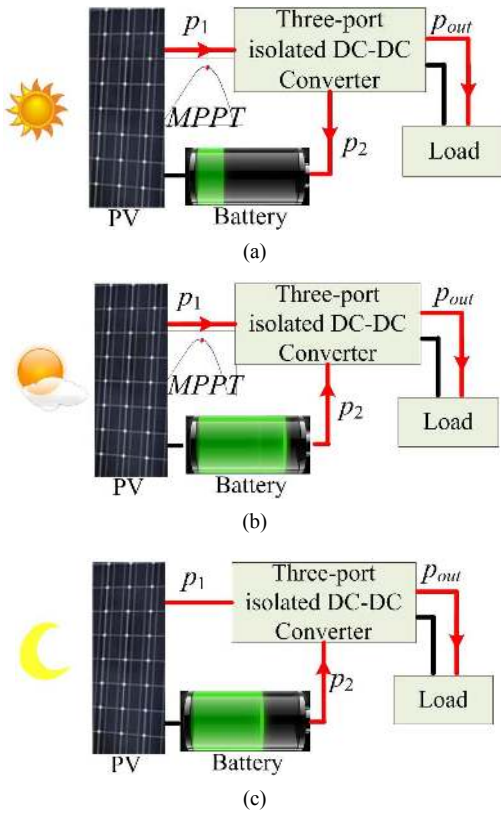
(a)

(b)

(c)

Fig. 5. Three working scenarios of the converter (The arrows show the directions of energy flow). (a) Scenario 1 ($p_1 > p_{out}$): PV works in MPPT mode and the battery works in charge mode to absorb the surplus solar energy; (b) Scenario 2 ($p_1 < p_{out}$): PV works in MPPT mode and battery works in discharge mode to provide the deficient energy; (c) Scenario 3 ($p_1 = 0$): there is no solar energy available and battery is discharged to supply load.

It can be seen that for the same power variation value, r_c is proportional to $1/P_1(k–1)$. In this paper, the switching period (T) will not be changed if the RPC is lower than a predefined value (e.g., 10^{-4}). As shown in Fig. 7, the P&O MPPT algorithm is realized by the frequency modulation method [22], where the conduction time of S_1, t_{on}, is fixed so that S_1 can achieve soft switching.

C. Charge and Discharge Controllers for Battery

Figs. 8(a) and (b) show the equivalent circuit of the battery and the converter when the battery works in the charge and discharge mode, respectively. To simplify the analysis, the battery is modeled as a capacitor C_b connected in series with its internal resistance r_b. Since C_b is sufficiently large, the terminal voltage of the battery, v_{bat}, can be calculated as $V_{boc} − i_{bat} \cdot r_b$, where V_{boc} is the open-circuit voltage of the battery. Then the transfer function between the battery current i_{bat} and the duty cycle d_2 of the switch S_2 in the charge mode can be derived:

$$G_c(s) = \frac{i_{bat}(s)}{d_2(s)} = \frac{(V_1 - V_{bat}) \cdot \left(s + \dfrac{1}{r_b \cdot C_2}\right)}{s^2 + \left(\dfrac{r_2}{L_2} + \dfrac{1}{r_b \cdot C_2}\right)s + \dfrac{r_2 / r_b + D_2}{L_2 \cdot C_2}} \quad (20)$$

where V_1 and V_{bat} represent the average voltages of the PV panel and the battery, respectively; r_2 and r_b represent the parasitic resistance of the inductor L_2 and the internal resistance
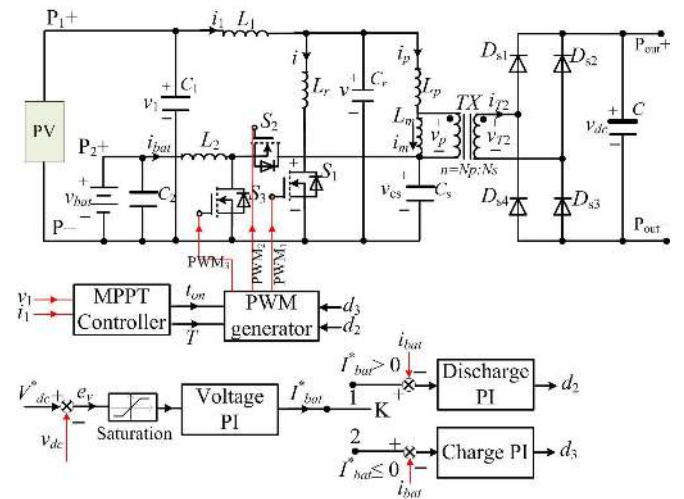

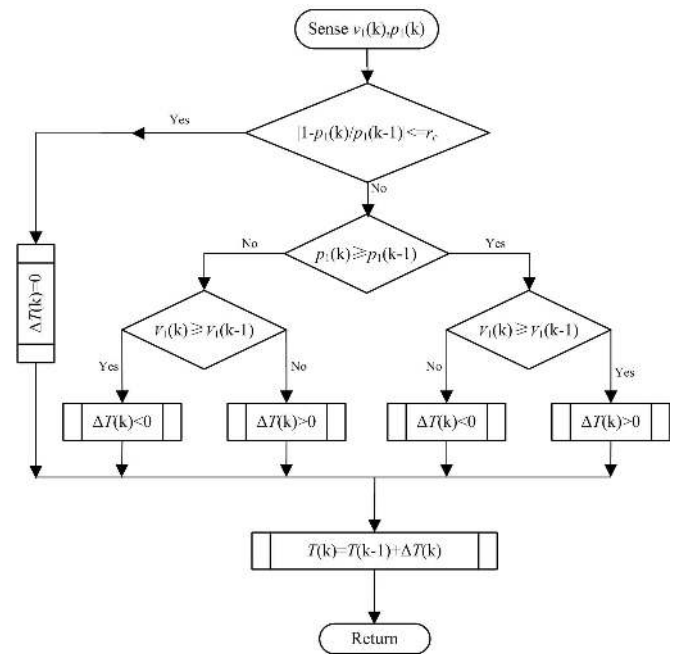Fig. 6. Overall block diagram of the system with controllers.

Fig. 7. The flowchart of the MPPT algorithm.
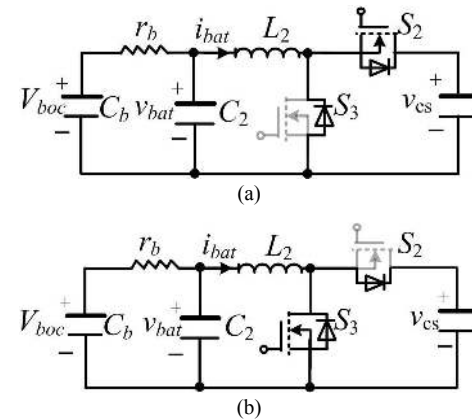

(a)

(b)

Fig. 8. Equivalent circuit of the battery with (a) the buck converter in charge mode and (b) the boost converter in discharge mode.

of the battery, respectively; D_2 is the steady-state value of the duty cycle of the switch S_2.

Similarly, the transfer function between i_{bat} and the duty cycle d_3 of the switch S_3 in the discharge mode is:

$$G_d(s) = \frac{i_{bat}(s)}{d_3(s)} = \frac{V_1 \cdot \left(s + \dfrac{1}{r_b \cdot C_2}\right)}{s^2 + \left(\dfrac{r_2}{L_2} + \dfrac{1}{r_b \cdot C_2}\right)s + \dfrac{r_2/r_b + 1}{L_2 \cdot C_2}} \quad (21)$$

To control the current of the battery, a proportional-integral (PI) controller, $K_p + K_i/s$, is used in the charge/discharge mode separately, as shown in Fig. 6. Each battery current PI controller takes the current error as the input to generate the duty cycle for S_2 or S_3 in the charge or discharge mode, respectively. When the reference current I^*_{bat} is zero or negative, the charge PI controller is selected such that $d_2 \geq 0$ and $d_3 = 0$. Otherwise, when the reference current I^*_{bat} is positive, the discharge PI controller is selected such that $d_3 > 0$

(a)

(b)

Fig. 9. Bode plots. (a) $i_{bat}(s)/d_2(s)$, and (b) $i_{bat}(s)/d_3(s)$.

and $d_2 = 0$.

The bode plots of $i_{bat}(s)/d_2(s)$ and $i_{bat}(s)/d_3(s)$ without the PI compensations (i.e., the open-loop transfer functions) are shown in Fig. 9. The plots imply that the two open-loop systems have low gains and 0 dB/decade slopes in the low-frequency region. Therefore, the design objective the PI compensation is to increase the low-frequency gains and make them cross the 0 dB line with a –20 dB/decade slope, while maintaining a sufficiently large phase margin (> 45º) and a high crossover frequency. By setting the crossover frequency in the range of one to several hundred Hz with a phase margin of 70º, the charge and discharge PI controllers can be derived. The bode plots of $i_{bat}(s)/d_2(s)$ and $i_{bat}(s)/d_3(s)$ with the PI compensations (i.e., the closed-loop transfer functions) are shown in Fig. 9 as well. After the compensations, the low-frequency gains have been increased and the low-frequency slopes are changed to be –20 dB/decade. The crossover frequencies corresponding to the charge and the discharge controllers are 300 Hz and 400 Hz, respectively.

Once the current controllers are designed, the outer-loop DC-link voltage controller which has a lower cutoff frequency than the current loop is then designed. The PI parameters of the current and voltage controllers used in this paper are listed in Table I.

Table I: Controller Parameters

	K_p	K_i
Current controller (charge)	2.5	5000
Current controller (discharge)	2.38	6600
Voltage controller	10	2

IV. SIMULATION RESULTS

Simulations are carried in MATLAB/Simulink to validate the proposed converter and the controllers. The parameters of the converter are as follows: transformer turn ratio n = 5:14, L_r = 3.3μH, L_p = 3.5 μH, and C_r = 0.22 μF. A SunWize SW-S55P PV panel is used, whose open-circuit voltage V_{oc} and the short-circuit current I_{sc} are 22 V and 3.15 A, respectively. The nominal voltage and internal resistance, r_b, of the battery are 7.5 V and 0.16 Ω, respectively. The on-time of the switch S_1, t_{on}, is 3 μs and the switching frequency varies in a range of 100 kHz to 170 kHz. The resistive load R_L = 100 Ω. The desired DC-link voltage, V^*_{dc}, and nominal power of the load are 50 V and 25 W, respectively.

To test the dynamic characteristic of the controllers, the solar radiation is step changed to examine the responses of the DC-link voltage and output power of the PV panel, as shown in Fig. 10. Fig. 10(a) shows that the initial solar radiation is zero and there is no power generated by the PV panel, as shown in Fig. 10(c). This indicates that the converter works in Scenario 1 and all of the power is supplied by discharging the battery. Fig. 10(b) shows that the DC-link voltage quickly reaches its reference value of 50 V.

Scenario 1 does not terminate until the solar radiation changes from zero to 400 W/m² at the 1st second. After that, the maximum power generated by the PV panel is 20 W, which is
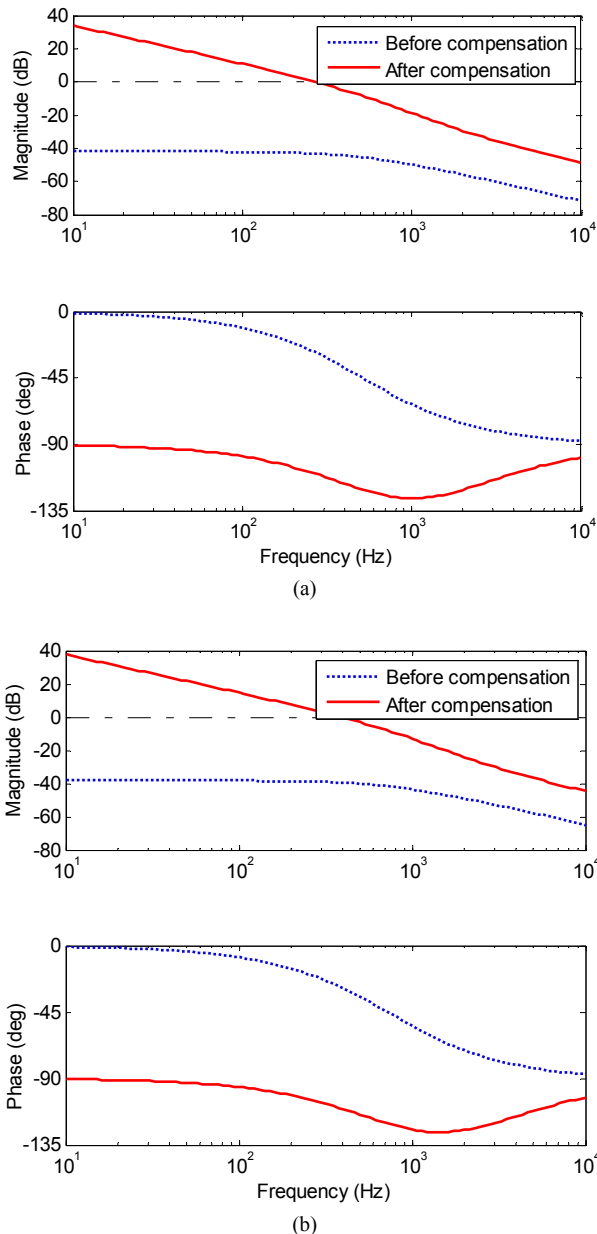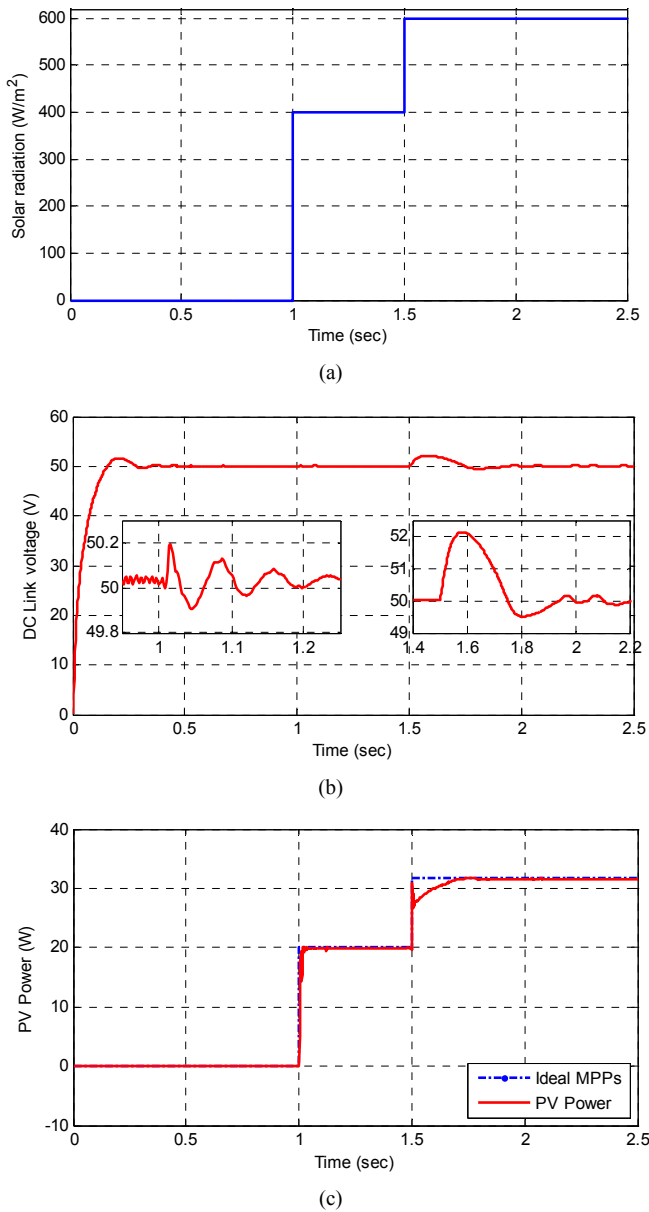
Fig. 10. Step responses. (a) The profile of solar radiation, (b) DC-link voltage response, and (c) PV power response.

less than the load demand of 25 W. Thus, the battery still works in the discharge mode to provide the deficient power required by the load and the variation of the DC-link voltage is negligible during the transition. From 1 second to 1.5 second, the converter works in Scenario 2. The PV panel generates the maximum power as indicated in Fig. 10(c).

At 1.5 second, the solar radiation is changed from 400 W/m^2 to 600 W/m^2, which corresponds to 32-W maximum power. Then the battery stops discharging and starts to absorb the surplus power generated by the PV panel. It takes some time to change the direction of the battery current, which not only results in an approximately 2-V overshoot in the DC-link voltage, but also leads to the PV power generated less than the ideal maximum power during the transient period, as shown in Fig. 10(c). After 0.3 seconds, both the DC-link voltage and PV power reach the desired value and the ideal maximum power
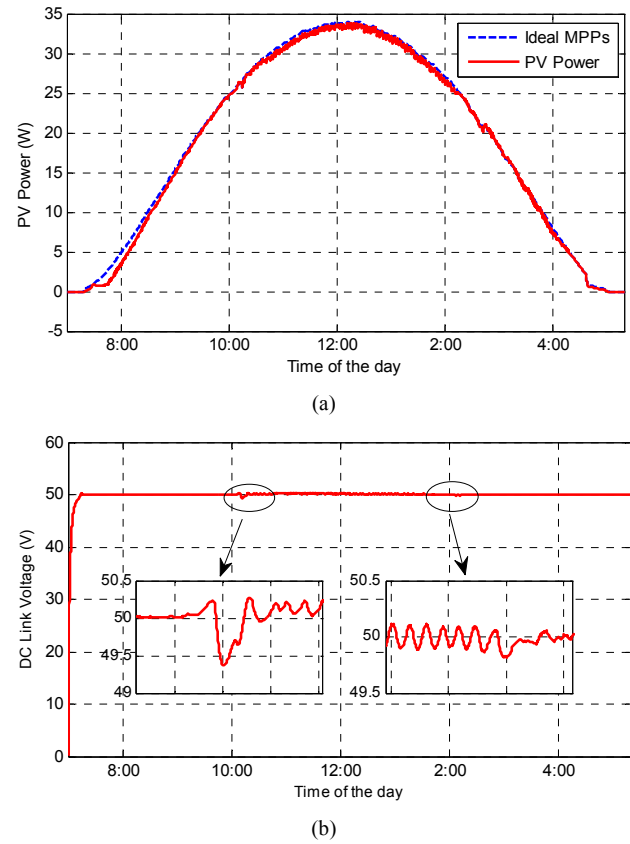

Fig. 11. Simulation results using the NREL data. (a) The generated PV power and (b) the DC-link voltage.

point (MPP), respectively.

To testify the effectiveness of the converter for MPPT control of the PV panel, real-world solar radiation data provided by the National Renewable Energy Laboratory (NREL) [23] was used. The data was collected from the South Table Mountain site in Golden, Colorado on Feb. 7, 2013. The duration of the dataset is 620 minutes with a resolution of one data point per minute. Fig. 11 shows the simulation results of the PV power and the DC-link voltage. As shown in Fig. 11(a), the energy extracted from the PV panel closely follows the ideal MPP by using the proposed converter and MPPT control algorithm. The DC-link voltage is well controlled at its desired value of 50 V. The maximum voltage error is approximately 1.2%, as shown in Fig. 10(b), which occurs around 10:10 am when the MPP increases to 25 W. At that time, the battery switches from the discharge mode to the charge mode. The steady-state voltage error is always less than 0.6%.

V. EXPERIMENTAL RESULTS

The system simulated is constructed in hardware to further validate the proposed converter and control algorithm via experimental studies. Fig. 12 shows the prototype of the whole system. It consists of the proposed DC-DC converter, which is connected to a SunWize SW-S55P PV panel, a battery, and an eZdsp F2812 control board. As shown in Fig. 12, the battery consists of four Samsung ICR18650-28A rechargeable lithium-ion cells, where two cells are connected in series to
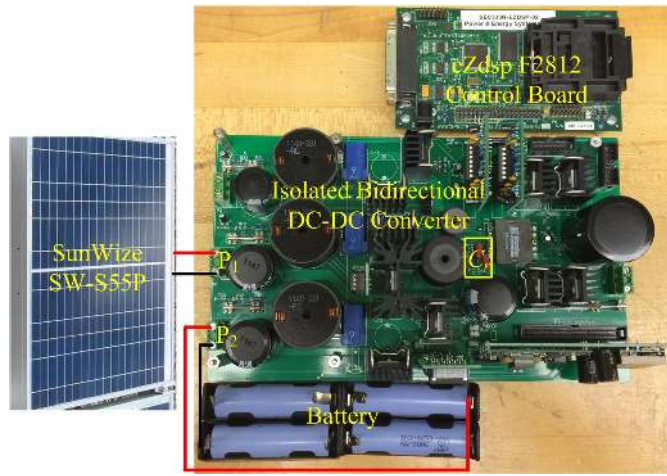
Fig. 12. The experimental system setup.

form a pack and two packs are connected in parallel. The nominal voltage, standard charging current, and capacity of the battery are 7.5 V, 2.8A, and 5600 mAh, respectively. The control algorithm is implemented in a TMS320F2812 DSP located on the control board. The parameters of the system are the same as those used in the simulation. Other parameters of the prototype converter are listed in Table II.

Table II: Component Specifications of the Prototype Converter.

| L_1, L_2	320 µH	C_1, C_2, C, C_s	1000 µF
L_m	75 µH	C_r	0.22 µF (100VDC)
L_r	3.3 µH	$Ds_1{\sim}Ds_4$	RHRP1540
L_{p1}	3.3 µH	S_1	IPB107N3
L'_p	0.2 µH	S_2, S_3	FDP3632

A. Steady-State Waveforms

Fig. 13 shows the steady-state waveforms of the resonant components, the switch S_1, and the transformer when Port 1 is connected to a 16 V voltage source. As shown in Fig. 13(a), when the switch S_1 is turned on, the voltage across C_r, v, decreases and the current through L_r and S_1, i, increases. The sinusoidal waveforms of v and i indicate the resonance between L_r and C_r. The current through the switch S_1 increases slowly such that it is turned on under a low di/dt (10 A/µs) condition. When the current drops to zero, the switch S_1 is fully turned off under the ZCS condition. Then the voltage across the switch S_1, v_{ds1}, is the same as that across the resonant capacitor C_r. The peak value of v_{ds1} is 35.8 V, which is approximately twice the input voltage. Fig. 13(b) shows the voltage (v_p) and current (i_p and i_{T2}) waveforms of the transformer. The direction of v_p is the same as i_{T2} regardless the state of the switch. This indicates that the power is delivered to the secondary side of the transformer in the entire switching period.

B. Voltage Regulation Ratio

Owing to the use of the LCL-resonant circuit, the frequency modulation method is used such that S_1 can achieve soft switching. The voltage regulation ratio, which is defined as V_T/V_1, is a function of the switching frequency when the frequency modulation method is used. Fig. 14 shows that the
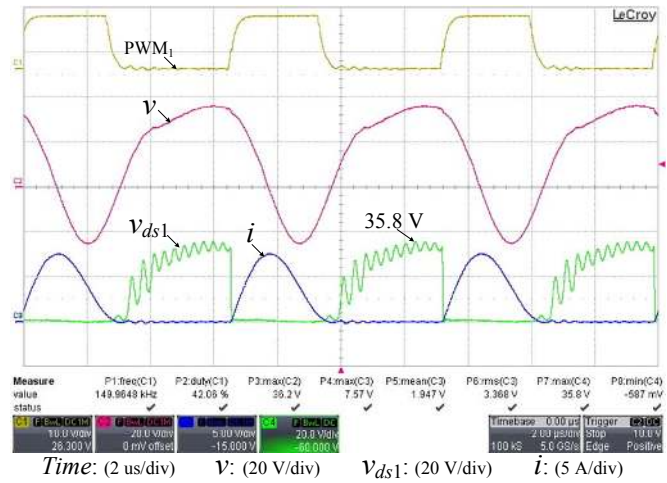
(a)
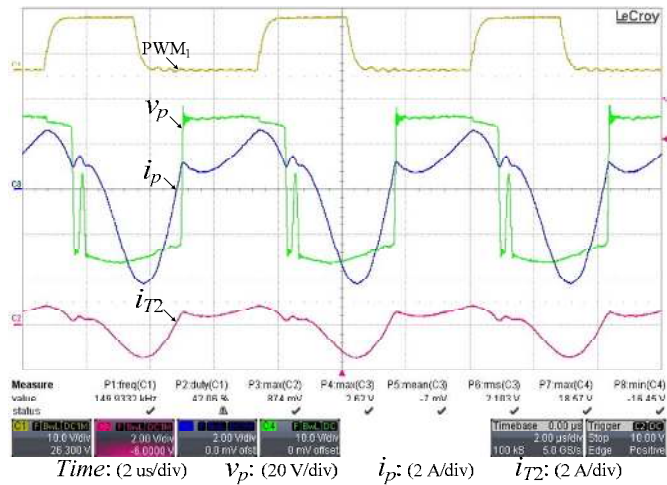
(b)

Fig. 13. The steady-state waveforms of the converter. (a) The voltage and current waveforms of the resonant components and (b) the voltage and current waveforms of the transformer.

voltage regulation ratio increases almost linearly with the normalized switching frequency f_s/f_r, where f_s and f_r are the switching frequency and the resonant frequency, respectively.

C. Three Scenarios

Fig. 15 shows the waveforms when the converter works in Scenario 1. As shown in Fig. 15(a), the power generated by the PV panel, p_1, in the steady state is 36.86 W, which is higher than the load power of 25 W. The negative battery current (i_{bat} = –0.87 A) indicates that the battery works in the charge mode. The DC-link voltage (v_{dc} = 50.18 V) is close to the reference value of 50 V, which demonstrates that the charge controller is effective to maintains a constant DC-link voltage. Fig. 15(b) shows the open-circuit transient responses of the voltage v_1, current i_1, and power p_1 of the PV panel when it is connected to Port 1. In the experiment, C_1 is initially fully discharged such that the initial value of v_1 is zero; the three switches S_1, S_2, and S_3 are off; and the controllers are deactivated. As shown in Fig. 15(b), v_1 increases from zero to its maximum value and i_1 decreases from a positive value to zero. As a result, p_1 first
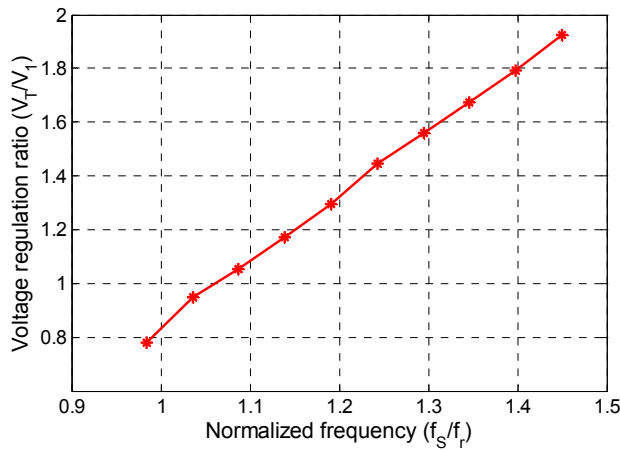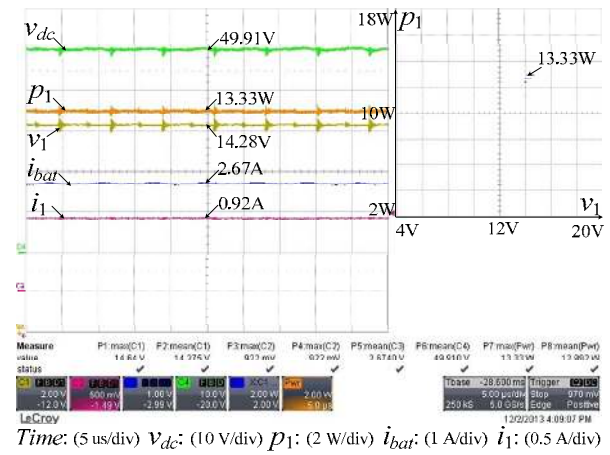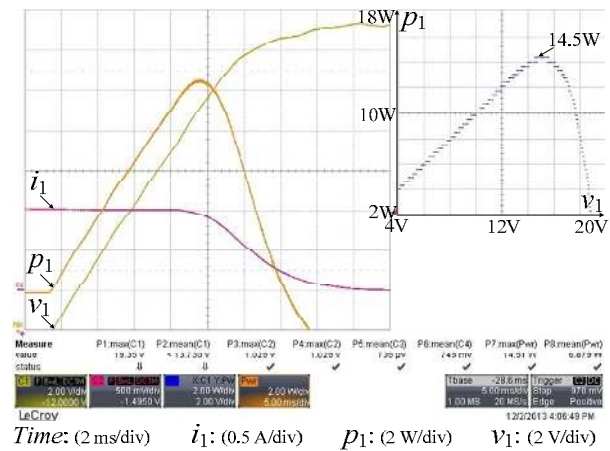
Fig. 14. Voltage regulation ratio as a function of the normalized frequency.

$Time$: (5 us/div) v_{dc}: (10 V/div) p_1: (2 W/div) i_{bat}: (1 A/div) i_1: (0.5 A/div)

(a)

$Time$: (10 us/div) p_1: (5 W/div) v_{dc}: (10 V/div) i_1: (1 A/div) i_{bat}: (0.5 A/div)

(a)

$Time$: (2 ms/div) i_1: (1 A/div) p_1: (5 W/div) v_1: (2 V/div)

(b)

Fig. 15. The waveforms when the converter works in Scenario 1. (a) The steady-state waveforms and (b) the P-V characteristic curve of the PV panel.

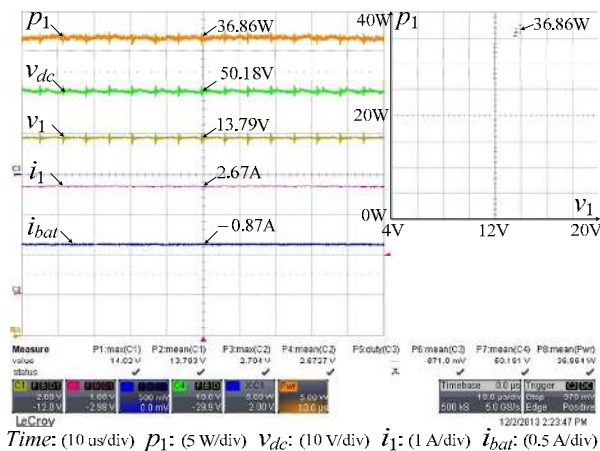$Time$: (2 ms/div) i_1: (0.5 A/div) p_1: (2 W/div) v_1: (2 V/div)

(b)

Fig. 16. The waveforms when the converter works in Scenario 2. (a) The steady-state waveforms; (b) the P-V characteristic curve of the PV panel.
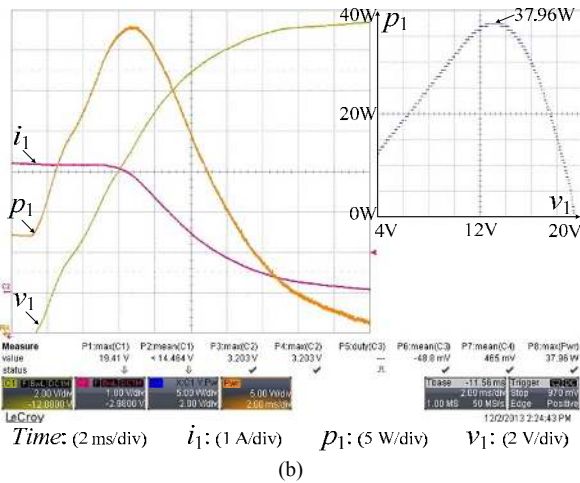

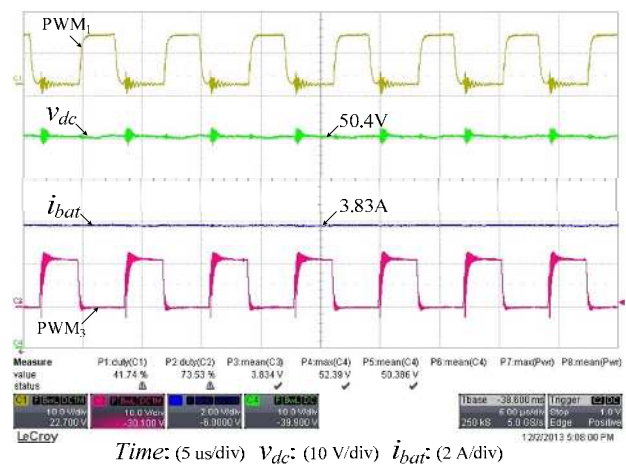$Time$: (5 us/div) v_{dc}: (10 V/div) i_{bat}: (2 A/div)

Fig. 17. The waveforms when the converter works in Scenario 3.

increases from zero to its MPP (37.96 W) and then decreases to zero. Based on the results, the power-voltage (P-V) characteristic curve of the PV panel can be generated, as shown on the right hand side of Fig. 15(b). It is assumed that the operating point of the PV panel does not change within three minutes since it was a clear day (Dec. 2, 2013 in Lincoln, NE). As shown in Fig. 15(b), the maximum power of the PV panel is

37.96 W, which is slightly higher than the measured mean value of 36.86 W in Fig. 15(a). Such a small deviation is caused by the P&O MPPT algorithm in which the duty cycle of the main switch S_1 varies slightly around the optimal duty cycle from time to time.

Fig. 16 shows the waveforms when the proposed converter

works in Scenario 2. As shown in Fig. 16(a), the power p_1 generated by the PV panel is 18.76 W, which is less than that required by the load. The positive battery current (i_{bat} = 1.42 A) indicates that the battery works in the discharge mode to supply the deficient power to the load. The DC-link voltage (v_{dc} = 50.4 V) is close to the reference value of 50 V, which demonstrates the DC-link voltage is well controlled by the discharge controller. Similarly, the measured PV power is also close to its maximum power 19.5 W shown in Fig. 16(b). Therefore, the proposed converter is capable of MPPT control for the PV panel as long as the solar energy is available.

Fig. 17 shows the steady-state waveforms of the converter when it works in Scenario 3. In this scenario, no solar energy is available. In the experiment, the PV panel was disconnected from Port 1. As shown in Fig. 17, the duty cycle of the switch S_1 is fixed around 0.42 and S_3 is active to form the boost converter to discharge the battery. The battery discharges with a current of 3.83 A, increasing from 1.42 A in Scenario 2. Therefore, the battery provides more energy in Scenario 3 than it does in Scenario 2. Meanwhile, the DC-link voltage is also well controlled at the desired value.

D. Comparison with the Hard-Switched Converter

A novelty or advantage of the proposed converter is that the main switch S_1 is turned off under the ZCS condition by using the LCL-resonant circuit implemented in Port 1. To testify the benefit of using the LCL-resonant circuit, the voltage stress of S_1 of the proposed converter is compared to that of the corresponding hard-switched converter, which is obtained by removing the LCL-resonant circuit L_r, C_r, and L_{p1} in the dash-line block of the proposed converter in Fig. 1. Fig. 18 shows the voltage and current waveforms of the switch S_1 of the hard-switched converter when V_1 = 16 V. As shown in Fig. 18, the gate signal is removed when the current of the main switch S_1 is 4 A; therefore, the main switch is not turned off under the ZCS condition and the peak voltage across the main switch is 65.9 V. When turning on the main switch, the value of di/dt in the hard-switched converter is 118 A/μs. In comparison, in the proposed converter, the main switch is turned off under the ZCS condition and the voltage stress and di/dt are reduced to 35.8 V and 10 A/μs, respectively, as shown in Fig. 13(a).

The efficiencies of the two converters are measured when the load is supplied by a voltage source connected to Port 1. Fig. 19 compares the measured efficiencies of the proposed soft-switched converter and the hard-switched converter. As shown in Fig. 19, the efficiencies of both converters first increase with the load power, reach the peak values when the load power is around 60 W, and then decrease with the load power when it is higher than 70 W. The proposed soft-switched converter always has a higher efficiency than the hard-switched converter and has achieved the peak efficiency of 94.5%.

VI. CONCLUSIONS

This paper has proposed a new isolated, three-port, bidirectional, DC-DC converter which uses the minimum number of switches. The proposed converter has been used for
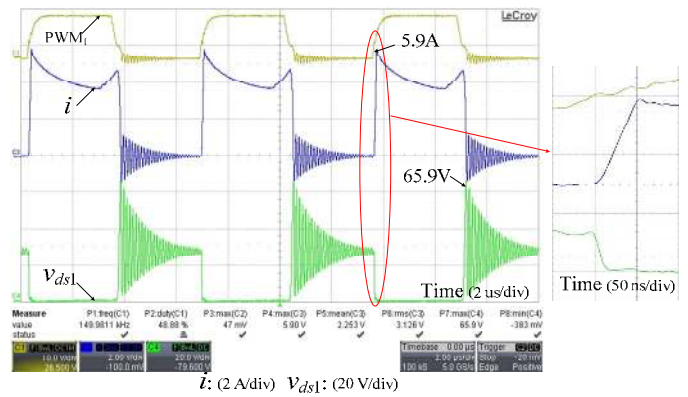

Fig. 18. The voltage and current waveforms of the switch S_1 in hard-switched converter.
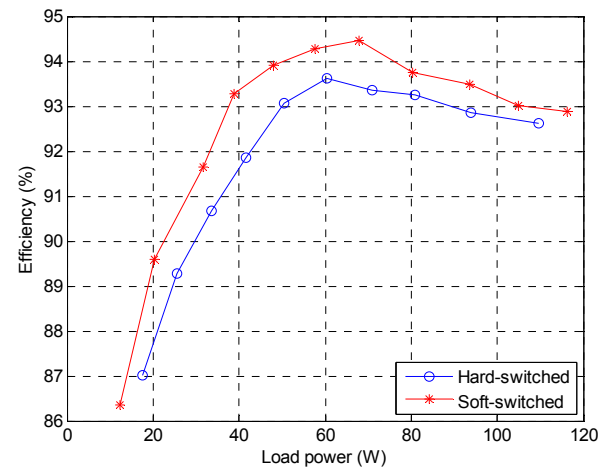

Fig. 19. Comparison of efficiency vs. load power of the proposed soft-switched converter and the hard-switched converter.

simultaneous power management of multiple energy sources, i.e., a PV panel and a battery, in this paper. Simulation results have shown that the converter is not only capable of MPPT for the PV panel when there is solar radiation, but also can control the charge/discharge of the battery to maintain the DC-link voltage at a constant value. Moreover, the voltage stress and the value of di/dt of the main switch have been reduced compared with the corresponding hard-switched converter. The proposed converter is applicable to other types of renewable energy sources, such as wind turbine generators.

REFERENCES

[1] C. Onwuchekwa and A. Kwasinski, "A modified-time-sharing switching technique for multiple-input DC-DC converters," *IEEE Trans. Power Electron.*, vol. 27, no. 11, pp. 4492-4502, Nov. 2012.

[2] A. Khaligh, J. Cao, and Y. Lee, "A multiple-input DC-DC converter topology," *IEEE Trans. Power Electron.*, vol. 24, no. 4, pp. 862-868, Mar. 2009.

[3] J. Lee, B. Min, D. Yoo, R. Kim, and J. Yoo, "A new topology for PV DC/DC converter with high efficiency under wide load range," in *Proc. European Conf. Power Electron. Appl.*, Sept. 2007, pp. 1-6.

[4] C. Lohmeier, J. Zeng, W. Qiao, L. Qu, and J. Hudgins, "A current-sensorless MPPT quasi-double-boost converter for PV systems," in *Proc. IEEE Energy Convers. Congr. Exposit.*, Sept. 2011, pp. 1069-1075.

[5]   K. Sayed, M. Abdel-Salam, A. Ahmed, and M. Ahmed, "New high voltage gain dual-boost DC-DC converter for photovoltaic power system," *Electr. Power Compon. Syst.*, vol. 40, no. 7, pp. 711-728, Apr. 2012.

[6]   Y. Chen, Y. Liu, and F. Wu, "Multi-input DC/DC converter based on the multi winding transformer for renewable energy applications," *IEEE Trans. Ind. Appl.*, vol. 38, no. 4, pp. 1096-1104, Aug. 2002.

[7]   Y. Jang and M. Jovanovic, "Isolated boost converter," *IEEE Trans. Power Electron.*, vol. 22, no. 4, pp. 1514-1521, Jul. 2007.

[8]   E. Yang, Y. Jiang, G. Hua, and F. Lee, "Isolated boost circuit for power factor correction," in *Proc. IEEE Appl. Power Electron. Conf. Exposit.*, Mar. 1993, pp. 196-203.

[9]   Y. Lembeye, V. Bang, G. Lefevre, and J. Ferrieux, "Novel half-bridge inductive DC-DC isolated converters for fuel cell applications," *IEEE Trans. Energy Convers.*, vol. 24, no. 1, pp. 203-210, Mar. 2009.

[10] J. Zeng, W. Qiao, L. Qu, and Y. Jiao, "An isolated multiport dc-dc converter for simultaneous power management of multiple different renewable energy sources," *IEEE J. Emerging Sel. Topics Power Electron.*, vol. 2, no. 1, pp. 70-78, Mar. 2014.

[11] H. Tao, A. Kotsopoulos, J. Duarte, and M. Hendrix, "Family of multiport bidirectional DC-DC converters," *IEE Proc. Electr. Power Appl.*, vol. 153, no. 3, pp. 451-458, May 2006.

[12] C. Zhao, S. Round, and J. Kolar, "An isolated three-port bidirectional DC-DC converter with decoupled power flow management," *IEEE Trans. Power Electron.*, vol. 23, no 5, pp. 2443-2453, Sept. 2008.

[13] J. Duarte, M. Hendrix, and M. Simoes, "Three-port bidirectional converter for hybrid fuel cell systems," *IEEE Trans. Power Electron.*, vol. 22, no. 2, pp. 480-487, Mar. 2007.

[14] G. Su and F. Peng, "A low cost, triple-voltage bus DC-DC converter for automotive applications," in *Proc. IEEE Appl. Power Electron. Conf. Exposit.*, Mar. 2005, pp. 1015-1021.

[15] D. Liu and H. Li, "A ZVS bi-directional DC-DC converter for multiple energy storage elements," *IEEE Trans. Power Electron.*, vol. 21, no. 5, pp. 1513-1517, Sept. 2006.

[16] H. Al-Atrash, F. Tian, and I. Batarseh, "Tri-modal half-bridge converter topology for three-port interface," *IEEE Trans. Power Electron.*, vol. 22, no. 1, pp. 341-345, Jan. 2007.

[17] Z. Qian, O. Abdel-Rahman, and I. Batarseh, "An Integrated four-port DC/DC converter for renewable energy application," *IEEE Trans. Power Electron.*, vol. 25, no. 7, pp. 1877-1887, Jul. 2010.

[18] B. Lu, W. Liu, Y. Liang, F.C. Lee, and J. Van Wyk, "Optimal design methodology for LLC resonant converter," in *Proc. IEEE Appl. Power Electron. Conf. Expo.*, Mar. 2006, pp. 1-6.

[19] J. Zeng, W. Qiao, and L. Qu, "A single-switch LCL-resonant isolated DC-DC converter," in *Proc. IEEE Energy Convers. Congr. Exposit.*, Sept. 2013, pp. 5496-5502.

[20] J. Zeng, W. Qiao, and L. Qu, "LCL-resonant single-switch isolated DC-DC converter," *IET Power Electron.*, to be published.

[21] C. Hua, J. Lin, and C. Shen, "Implementation of a DSP-controlled photovoltaic system with peak power tracking," *IEEE Trans. Ind. Electron.*, vol. 45, no. 1, pp. 99-107, Feb. 1998.

[22] B. York, W. Yu, and J. Lai, "Hybrid-frequency modulation for PWM-integrated resonant converters," *IEEE Trans. Power Electron.*, vol. 28, no. 2, pp. 985-994, Feb. 2013.

[23] http://www.nrel.gov/midc/apps/go2url.pl?site=BMS&page=day.pl?BMS

[24] J. Zeng, W. Qiao, and L. Qu, "A single-switch isolated dc-dc converter for photovoltaic systems," in *Proc. IEEE Energy Convers. Congr. Exposit.*, Raleigh, NC, Sept. 2012, pp. 3446-3452.

uninterruptible power supplies. His research interests include power electronics, renewable energy, microgrids, and computational intelligence for electric power and energy systems.

Wei Qiao (S'05–M'08–SM'12) received the B.Eng. and M.Eng. degrees in electrical engineering from Zhejiang University, Hangzhou, China, in 1997 and 2002, respectively, the M.S. degree in high performance computation for engineered systems from Singapore-MIT Alliance (SMA), Singapore, in 2003, and the Ph.D. degree in electrical engineering from Georgia Institute of Technology, Atlanta, GA, USA, in 2008.

Since August 2008, he has been with the University of Nebraska—Lincoln (UNL), USA, where he is currently an Associate Professor in the Department of Electrical and Computer Engineering. His research interests include renewable energy systems, smart grids, microgrids, condition monitoring and fault diagnosis, energy storage systems, power electronics, electric machines and drives, and computational intelligence. He is the author or coauthor of 3 book chapters and more than 140 papers in refereed journals and international conference proceedings and has 5 international/U.S. patents pending.

Dr. Qiao is an Associated Editor of the IEEE Transactions on Energy Conversion, the IET Power Electronics, and the IEEE Journal of Emerging and Selected Topics in Power Electronics, and the Corresponding Guest Editor of a special section on Condition Monitoring, Diagnosis, Prognosis, and Health Monitoring for Wind Energy Conversion Systems of the IEEE Transactions on Industrial Electronics. He was an Associate Editor of the IEEE Transactions on Industry Applications in 2010-2013. He was the recipient of a 2010 U.S. National Science Foundation CAREER Award, the 2010 IEEE Industry Applications Society (IAS) Andrew W. Smith Outstanding Young Member Award, the 2012 UNL College of Engineering Faculty Research & Creative Activity Award, the 2011 UNL Harold and Esther Edgerton Junior Faculty Award, and the 2011 UNL College of Engineering Edgerton Innovation Award. He has received four best paper awards from IEEE IAS, PES, and PELS.
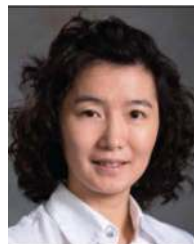
Liyan Qu (S'05–M'08) received the B.Eng. (with the highest distinction) and M.Eng. degrees in electrical engineering from Zhejiang University, Hangzhou, China, in 1999 and 2002, respectively, and the Ph.D. degree in electrical engineering from the University of Illinois at Urbana–Champaign, USA in 2007.

From 2007 to 2009, she was an Application Engineer with Ansoft Corporation. Since January 2010, she has been with the University of Nebraska—Lincoln (UNL), where she is currently an Assistant Professor in the Department of Electrical and Computer Engineering. Her research interests include energy efficiency, renewable energy, numerical analysis and computer aided design of electric machinery and power electronic devices, dynamics and control of electric machinery, permanent-magnet machines, and magnetic materials.

Jianwu Zeng (S'10) received the B.Eng. degree in electrical engineering from Xi'an University of Technology, Xi'an, China, in 2004, and the M.S. degree in control science and engineering from Zhejiang University, Hangzhou, China, in 2006. Currently, he is working toward the Ph.D. degree in electrical engineering with the University of Nebraska-Lincoln, USA.

In 2006, he joined Eaton Electrical (Shenzhen) Company, Ltd., Shenzhen, China, where he was an Electronic Engineer involved in research and development on soft-switching and bidirectional DC-DC converters for